Huang et al. *NPG Asia Materials* (2026)18:8
https://doi.org/10.1038/s41427-026-00641-y

NPG Asia Materials

ARTICLE Open Access

Aerosol assisted chemical vapor deposition of cobalt-based co-catalysts on bismuth vanadate-based photoelectrodes for solar water splitting systems

Mengyuan Huang[1], George Creasey[1,2], Zhipeng Lin[1], Anna Hankin[2], Brian Tam[1] and Andreas Kafizas[1,3]

Abstract

Cobalt phosphate (CoPi) is a widely used oxygen evolution reaction (OER) catalyst in photoelectrochemical (PEC) water splitting systems. Traditionally, CoPi is fabricated via photo-assisted electrodeposition (PED) from a cobalt-containing electrolyte solution, a method that is limited in scalability. In this study, we demonstrate a novel and scalable route to CoPi, where cobalt oxide (CoO_x) is first grown by aerosol-assisted chemical vapour deposition (AACVD) and then surface modified through a dark electrochemical treatment (ET) process. Both fabrication techniques were used to deposit CoPi onto bismuth vanadate ($BiVO_4$) photoanodes synthesised by AACVD. CoPi-decorated $BiVO_4$ fabricated *via* AACVD + ET demonstrated superior charge separation efficiency, stability over four hours of chronoamperometry, and photoelectrochemical performance, achieving an improved half-cell solar-to-hydrogen (HC-STH) efficiency of 1.16% at 1.23 V vs RHE compared to CoPi-decorated $BiVO_4$ fabricated by PED, which exhibited an HC-STH efficiency of 0.60%. These promising results highlight the potential of AACVD, conducted under atmospheric pressure, to enable the future development of both co-catalysts and scalable photoelectrode fabrication for large-area applications.

Introduction

The excessive use of fossil fuels to meet global demands have increased carbon dioxide (CO_2) emissions that are the primary cause of global warming[1]. Hydrogen (H_2) is a clean energy carrier already used at an industrial scale, but that is almost wholly produced from fossil fuels today[2]. Solar driven (photocatalytic) water splitting has emerged as a particularly promising strategy that mimics natural photosynthesis by using semiconductor materials to absorb sunlight and split water into oxygen and renewable hydrogen.

Among n-type metal oxide semiconductors for photoelectrochemical (PEC) water oxidation–including titania (TiO_2), hematite (α-Fe_2O_3), and tungsten trioxide (WO_3)–bismuth vanadate ($BiVO_4$) stands out due to its visible light active bandgap (~2.4 eV) and its resistance to photocorrosion in neutral and basic electrolytes[3]. Under AM1.5 G sunlight, $BiVO_4$ has a theoretical maximum solar-to-hydrogen (STH) efficiency of 9.2% and photocurrent density of 7.5 mA cm^{-2}.

Although $BiVO_4$ has relatively low electron (~10 nm)[4] and hole (~100 nm)[5] diffusion lengths that can lead to high electron/hole recombination losses, these can be countered by materials design strategies, such as the formation of type-II staggered heterojunctions[6]. Spectroscopic studies show that bare $BiVO_4$ requires 20–100 µs for electron extraction to occur, whereas the addition of a WO_3 layer in a heterojunction enables sub-microsecond transfer into the WO_3 conduction band[7], improving overall PEC performance.

Correspondence: Brian Tam (b.tam18@imperial.ac.uk) or Andreas Kafizas (a.kafizas@imperial.ac.uk)
[1]Department of Chemistry, Molecular Sciences Research Hub, Imperial College London, London, UK
[2]Department of Chemical Engineering, Imperial College London, South Kensington, London, UK
Full list of author information is available at the end of the article

To improve the extraction of holes from $BiVO_4$, catalytic materials that drive the oxygen evolution reaction (OER) such as cobalt oxides (CoO_x) and cobalt phosphate (CoPi) have emerged as particularly promising non-precious metal candidates. In 2015, Ma et al. reported that surface modification of $BiVO_4$ with CoPi resulted in a cathodic shift of the photocurrent onset potential by approximately 200–300 mV[8]. The performance enhancement was attributed to suppression of back electron/hole recombination, where CoPi accumulates long-lived holes at the $BiVO_4$ surface[8–10]. During OER, redox cycling of cobalt between Co^{2+} to Co^{3+} enables a self-repair mechanism, improving stability during long-term operation[11,12]. In 2023, Varma et al. reported the fabrication of Fe-doped CoO_x co-catalyst layers on $BiVO_4$ photoanodes via photo-assisted electrodeposition (PED). Their optimised photoanode achieved a photocurrent density of 4.6 mA cm^{-2} at 1.23 V_{RHE}[13]. Similarly, in 2022, Fang et al. used electrodeposition (ED) to deposit CoPi on $BiVO_4$, resulting in a photocurrent density of 5.87 mA cm^{-2} and a marked cathodic shift in the onset potential from 0.45 V_{RHE} to 0.20 V_{RHE} [14].

Deposition via PED requires illumination and applied bias, which may be limited in scalability, and additionally requires that the electrolyte will not attenuate the illumination. Hence, we propose a more scalable alternative, where aerosol assisted chemical vapour deposition (AACVD) is used to deposit CoO_x that is subsequently converted into CoPi through dark electrochemical treatment (ET). Moreover, by growing the $BiVO_4$ layers using the AACVD method as well, this versatile technique may be used to produce all layers in the PEC system. In this study, we optimise the surface modified CoPi, and to benchmark this method, CoPi is fabricated using the conventional PED approach on AACVD-fabricated substrates.

Materials and methods

Experimental methods are briefly outlined here with further details presented in the Supplementary Information.

Chemical vapour deposition of photoanodes and cobalt oxide

The AACVD system utilised in this study is featured in several publications[15–17]. Briefly, 1.3 × 2.5 cm^2 area and 3 mm thick FTO-coated glass substrates (TEC 15, Pilkington NSG) were first cleaned by successive sonication for 10 min each in deionised water with detergent, deionised water (18.2 MΩ cm, Sartorius), acetone (Technical, VWR Chemicals), and finally methanol (Reag. Ph.Eur., ACS, VWR Chemicals)[16]. In a typical $BiVO_4$ deposition, vanadium (III) acetylacetonate (0.2 mmol, 0.0700 g, 97%, Sigma-Aldrich) and triphenyl bismuth (0.2 mmol, 0.0881 g, 98%, Santa Cruz Biotechnology Inc.) were dissolved in 40 mL of a 3:1 methanol:acetone mixture, aerosolised using an ultrasonic humidifier (2 MHz, Liquifog, Johnson Matthey), and carried using compressed air at a flow rate of 1.5 L min^{-1} over FTO substrates heated to 400 °C. The as-deposited $BiVO_4$ films were finally annealed at 500 °C in air for 2 h. $WO_3/BiVO_4$ heterojunction fabrication was conducted by depositing $BiVO_4$ onto pre-synthesised nanoneedle (NN) WO_3 films, while the flat heterojunction system was formed by depositing $BiVO_4$ on flat WO_3 films, as reported elsewhere[15]. For a typical CoO_x deposition on FTO, cobalt (II) acetylacetonate ($Co(acac)_2$) (0.0257 g, 0.1 mmol, 5 mM, 98%, Fluorochem) was dissolved in 20 mL of ethanol (absolute >= 99%, Fisher Scientific) and delivered by compressed air carrier gas flow rate of 1.5 L min^{-1} over substrates heated to 400 °C.

Electrochemical treatment (ET) of CoO_x to form CoPi

ET of CoO_x to form CoPi was performed by immersing CoO_x films into pH 7, 0.1 M aqueous potassium phosphate (KPi) (K_2HPO_4/KH_2PO_4, 99%, Thermo Scientific) buffer under an applied potential of 1.5 V_{RHE} in the dark. An AgCl/Ag (saturated KCl) electrode served as the reference electrode and a platinum mesh as the counter electrode. Chronoamperometry lasting 10 minutes (resulting in a total charge transfer of ~0.8 mC cm^{-2}) was applied (Supplementary Information Fig. S1) converting cobalt oxide into cobalt phosphate through cobalt ion dissolution–redeposition from the electrolyte [11].

Photoelectrochemical deposition (PED) of CoPi

PED of CoPi[18] was carried out using white light illumination from a 75 W xenon lamp (Hamamatsu) in a quartz cuvette (5 cm × 3 cm × 13 cm). Cobalt nitrate (0.0146 g, 0.5 mM, 98%, Fluorochem) was dissolved in 100 mL of either pH 7 0.1 M KPi buffer electrolyte for CoPi deposition or borate buffer (1 M H_3BO_3, >=99.5%, Sigma Life Science, adjusted to pH 9) electrolyte for CoO_x deposition for comparison. Electrodeposition was performed under three cycles of constant current conditions (20 μA cm^{-2}). Between each cycle, the system was held at open circuit potential (OCP) of 0.61 V_{RHE} for 260 s.

Physical characterisation methods

Thermogravimetric analysis (TGA) was performed using a Mettler Toledo TGA/DSC 1LF/UMX system, coupled with a Hiden Analytical HPR-20 QIC Evol mass spectrometer. SEM images & energy-dispersive X-ray spectroscopy (EDX) were acquired using a Zeiss Sigma microscope operating at 5 kV, equipped with an InLens detector. X-ray diffraction (XRD) measurements were carried out using a Bruker D2 Phaser diffractometer equipped with parallel beam optics and a Lynx-Eye

detector. Raman spectra were collected using a DXR3® Raman Microscope (Thermo Fisher Scientific) with a laser wavelength of 532 nm. UV-Visible (UV–vis) transmittance and reflectance spectra were measured using a UV-2600 Shimadzu spectrophotometer equipped with an integrating sphere. X-ray photoemission spectroscopy (XPS) was measured with a Thermo Fisher K-Alpha+ with a monochromated Al Kα X-ray source. X-ray fluorescence (XRF) was measured using a Malvern Panalytical Epsilon 3 spectrometer.

Photoelectrochemical water splitting measurements

PEC linear sweep voltammetry and incident photon-to-electron conversion efficiency measurements were performed with an Autolab PGSTAT101 potentiostat and Nova software in a standard three-electrode configuration. An AgCl/Ag (saturated KCl) reference electrode was used, platinum mesh served as the counter electrode, and a phosphate-free 1 M, pH 9 borate aqueous buffer solution was the electrolyte. This buffer was selected to provide a distinct electrochemical environment from the phosphate-based electrolyte used during electrochemical treatment, which converts the surface of the (AACVD)-fabricated CoO_x into CoPi. Illumination was provided by a 75 W xenon lamp attenuated with a KG3 filter. The intensity of this white light source was measured by UV–vis and NIR spectrophotometers to be 44% of the light intensity of the AM 1.5 G solar spectrum, and so measured photocurrents are plotted scaled to 1-sun illumination, given that photocurrents of $BiVO_4$ have been shown to scale linearly at this regime [9].

The incident photon-to-current efficiency (IPCE) was determined by measuring the photocurrent response at discrete wavelengths ranging from 275 to 550 nm in 25 nm intervals using a monochromator (OBB-2001, Photon Technology International). During each measurement, a constant potential of 1.23 V_{RHE} was applied. The incident light intensity at each wavelength was calibrated using a Thorlabs optical power metre (PM100D) equipped with an S120VC photodiode sensor.

Further photoelectrochemical impedance spectroscopy (PEIS), stability measurements, and charge separation and injection efficiency measurements were conducted under one sun illumination with a Class A Sun2000 Solar Simulator (Abet Technologies), equipped with a 550 W Xe lamp and AM 1.5 G filter. The light spectrum and intensity were characterised by StellarNet Black Comet UV/vis (280–900 nm) spectrophotometers, interfaced with SpectraWiz software. The measured light spectrum was compared with the NREL AM 1.5 G reference spectrum[19] and the working distance was adjusted such that the cumulative light intensity over the measured region was equivalent to AM 1.5 G (one sun). A representative spectrum of the Sun2000 solar simulator is provided in Fig. S2. These photoelectrochemical tests were carried out using a three-electrode setup in a (quiescent) FC PEC H-Cell 2 × 15 mL - Front Contact Photo-Electrochemical H-Cell (Redox.me). The working electrode potential was controlled by an Autolab PGStat302N potentiostat (Metrohm). Electrode potentials were referenced with Redox.me refillable AgCl/Ag reference electrodes (sat. KCl, 0.197 V_{SHE} at 25 °C) and a Redox.me Pt auxiliary electrode was used.

Photoelectrochemical impedance spectroscopy (PEIS) measurements were conducted to investigate the effect of the co-catalysts on bulk resistance. Frequencies of 10^5 to 10^{-1} (10 points per decade) were used with a constant applied electrode potential of 0.8 V ± 10 mV. PEIS data was processed using Nova 2.1.8 (Autolab). The equivalent circuit shown in Fig. S3 was selected for the analysis.

Results and discussion

AACVD of cobalt oxide and subsequent electrochemical treatment

During AACVD, substrate temperature directly influences the thermal decomposition of the precursor and resulting film composition. The TGA profile of cobalt (II) acetylacetonate ($Co(acac)_2$) in air (Fig. 1a) shows an initial weight loss of 6 wt% between 30 °C and 100 °C, corresponding to loss of surface adsorbed water. A gradual weight loss from 100 °C to 140 °C followed by a significant mass reduction between 140 °C and 230 °C is correlated to acac ligand expulsion. Combustion of residual carbonaceous species occurs up to 400 °C, after which the weight stabilises at a residual mass of approximately 10 wt%. Although this value is lower than would be expected from the molecular weights, melting and subsequent boiling of $Co(acac)_2$ occurs at 165–170 °C and 215 °C respectively, concurrent with decomposition, explaining the non-stoichiometric mass loss. Accordingly, 400 °C was selected for all subsequent (AACVD)-CoO_x depositions to ensure complete conversion of the cobalt precursors into the oxide.

Top-down and side-on SEM images for (AACVD)-CoO_x on FTO are shown in the Supplementary Information Fig. S4a and S4b. The CoO_x particles exhibit distinct angular facets, which are likely indicative of cubic CoO crystallites, such as those described by Melze et al[20]. Fig. 1b, c present top-down and side-on SEM images for the (AACVD + ET)-CoPi deposited on FTO from 5 mM precursor solution, showing an 85 nm thick layer on FTO and no visible changes from the 75 nm thick (AACVD)-CoO_x samples, which is consistent with surface phosphate modification of the CoO_x film. The resulting surface roughness and cross-sectional crystallite morphology may be a function of the FTO surface roughness.

Furthermore, XRD patterns, Raman spectroscopy, energy-dispersive X-ray spectroscopy (EDX) and X-ray

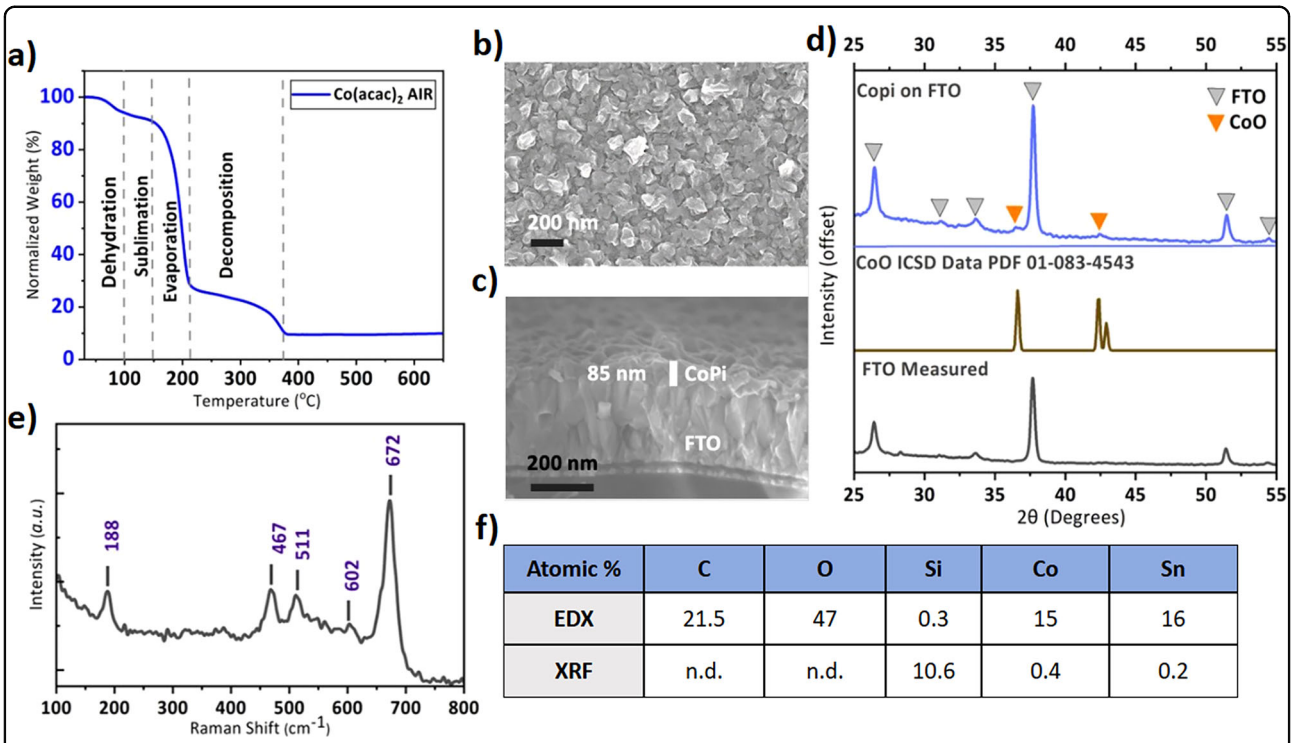

Atomic %	C	O	Si	Co	Sn
EDX	21.5	47	0.3	15	16
XRF	n.d.	n.d.	10.6	0.4	0.2

Fig. 1 Analysis of a representative (AACVD + ET)-CoPi fi lm on FTO. Analysis of a representative (AACVD + ET)-CoPi film on FTO deposited from a 5 mM $Co(acac)_2$ precursor solution in 20 mL of ethanol at 400 °C and treated with 1.5 V_{RHE} chronoamperometry for 10 min in KPi buffer solution. **a** TGA for the $Co(acac)_2$ precursor, **b** Top-down and **c** Side-on SEM images, **d** XRD patterns, **e** Raman spectrum, and **f** EDX and XRF atomic % determination (n.d. not determinable).

fluorescence (XRF) of the (AACVD + ET)-CoPi samples were measured. In Fig. 1d, e, the XRD pattern shows peaks near 36 and 42 degrees two theta corresponding to cobalt oxide (CoO). The CoO_x deposited herein by AACVD at a substrate temperature of 400 °C shows Raman peaks at 188, 467, 511, 602 and 672 cm^{-1} that are fully consistent with the Raman peak shifts for Co_3O_4 reported in the literature as having been prepared by the aerosol-assisted pyrolysis of cobalt acetate tetrahydrate between 250 and 350 °C[21]. This reported technique is similar to the AACVD investigated in this work, with nanopowders synthesised by pyrolysis in a tube furnace. The higher temperature required for AACVD may be a result of the surface heating orientation as the film is formed. The Raman peak shifts ranged from 184 to 191, 462 to 469, 508 to 511, 596 to 506, and 659 to 675 cm^{-1} respectively, indicating the AACVD material was closer in similarity to the Co_3O_4 prepared at 350 °C[21]. These peaks correspond to the Raman-active $3F_{2g}$, E_g, $2F_{2g}$, $1F_{2g}$, and A_{1g} vibrational modes respectively, and are red shifted compared to Co_3O_4 standard[22] which, along with bandwidth broadening, is indicative of decreased crystallite size[21]. The XRD data indicate the presence of CoO although the peaks are weak and do not exclude the presence of more amorphous Co_3O_4 phases. Raman spectroscopy more clearly shows features specific to Co_3O_4, but the Raman spectrum of CoO is characterised by a broad feature between 450 and 600 cm^{-1}[22], which is possibly also present in the measurement. Ultimately, the catalyst may plausibly consist of a mixed phase with CoO and Co_3O_4. Catalytic performance reflects the state of the surface layer undergoing catalysis, but the specific stoichiometry would be expected to fluctuate under varying applied potentials. EDX (Fig. S5) and XRF (Fig. S6) spectra for (AACVD + ET)-CoPi (elemental abundance tabulated in Fig. 1f), show signals for cobalt and oxygen, indicating the successful synthesis of a cobalt oxide overlayer. The X-rays used in EDX were accelerated at 15 kV and up to 50 kV for XRF and hence the sample space analyzed is deeper (within the glass substrate) for the XRF measurements compared to for the EDX measurements. However, phosphate incorporation was undetectable by these methods. Figures S7 and S8 show XPS spectra and fitting tables of representative samples of (AACVD)-CoO_x and (AACVD + ET)-CoPi on FTO. For (AACVD)-CoO_x, XPS indicates cobalt is present as a 1:3 mixture of Co^{2+} and Co^{3+}, identified with the XPS peak associated with Co^{2+} having an atomic ratio of 1:0.9 to oxygen associated with Co^{2+}, and the peak associated with Co^{3+} having a ratio of 1:1.2 to oxygen associated with Co^{3+}. After

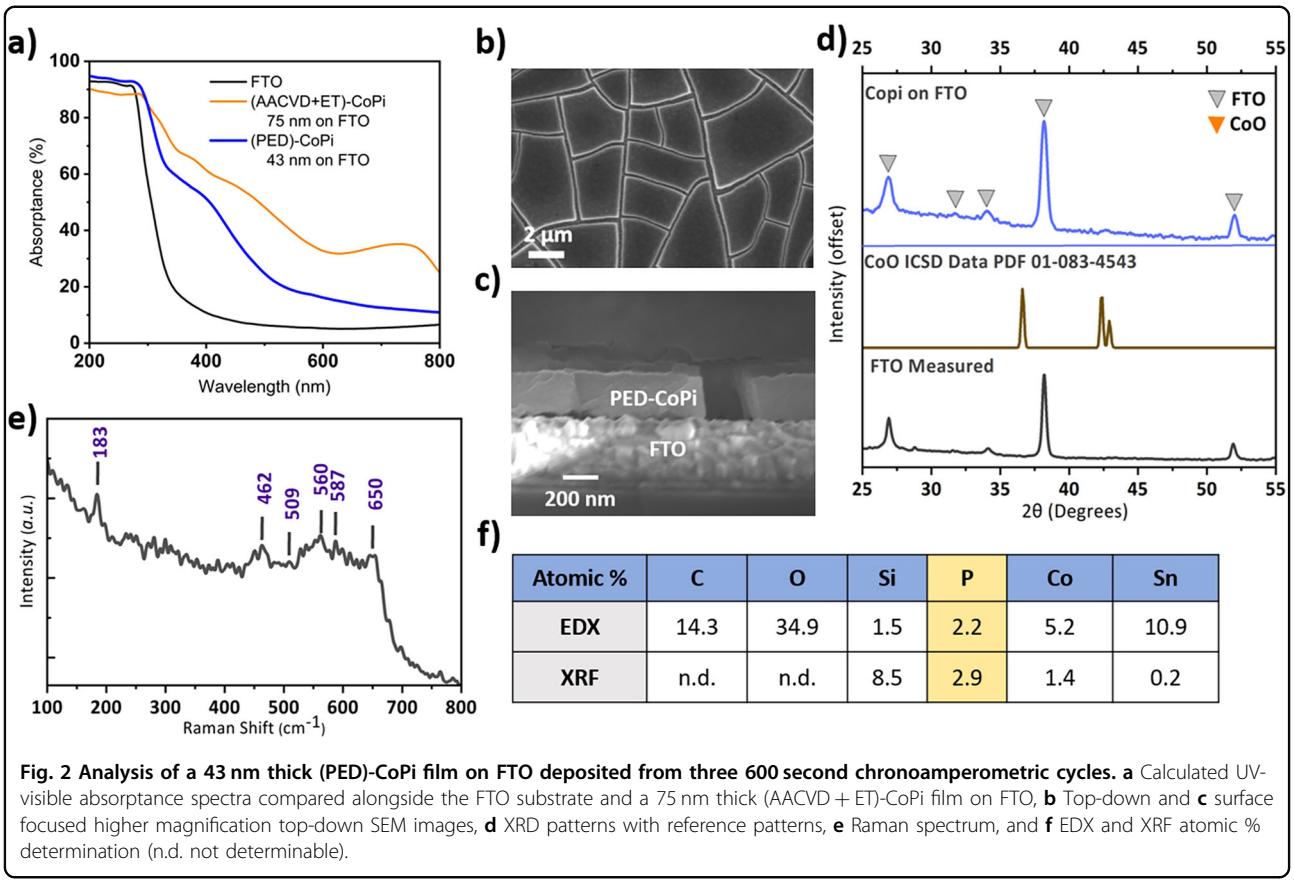

Atomic %	C	O	Si	P	Co	Sn
EDX	14.3	34.9	1.5	2.2	5.2	10.9
XRF	n.d.	n.d.	8.5	2.9	1.4	0.2

Fig. 2 Analysis of a 43 nm thick (PED)-CoPi film on FTO deposited from three 600 second chronoamperometric cycles. a Calculated UV-visible absorptance spectra compared alongside the FTO substrate and a 75 nm thick (AACVD + ET)-CoPi film on FTO, **b** Top-down and **c** surface focused higher magnification top-down SEM images, **d** XRD patterns with reference patterns, **e** Raman spectrum, and **f** EDX and XRF atomic % determination (n.d. not determinable).

electrochemical treatment in phosphate buffer, the (AACVD + ET)-CoPi shows the presence of atomic 1.4 ± 0.4% phosphorous with a binding energy of 133 eV. The uncertainty is calculated from the residual standard error between the fitted curve and measurement data points, which is calculated to be 17 counts s^{-1} (Fig. S8). The standard error in the peak area is then 93 counts s^{-1}, where the total area of the P 2p peak is 335 counts s^{-1} integrated over 5.5 eV of binding energy. As XPS is a surface sensitive technique (i.e. it probes up to ~10 nm), this result indicates that only the surface of the cocatalyst contains phosphate and explains why phosphorous is undeterminable by EDX or XRF analysis, as these techniques primarily probe the bulk (i.e. several microns deep). This limited conversion is consistent with the limited charge passed during chronoamperometry of ~0.8 mC cm^{-2} (Fig. S1). As detailed in the Supplementary Information, the charge passed is estimated to equal to a layer of CoPi 1.5 nm thick.

Photoelectrodeposition (PED) of CoPi from cobalt-containing solutions

CoPi deposited by PED over three 100 s, 600 s, and 3000 s chronopotentiometric repetitions are calculated to be 7 nm, 43 nm, and 217 nm thick according to side-on SEM imaging, discussed below. These values and their corresponding current densities are tabulated in Table S1. In Fig. 2a, the UV-visible absorptance calculated from transmittance and total reflectance measurements for 43 nm thick (PED)-CoPi on FTO has the same trend as 75 nm thick (AACVD + ET)-CoPi on FTO, with both having broad absorption and being brown in colour. In Fig. 2b, c, the top-down and side-on SEM images of (PED)-CoPi deposited from three 3000-s chronoamperometry cycles show that CoPi forms very flat, uniform and dense plates on the nanoscale, but with deep cracks between these plates seen on the micron-scale that reach down to the FTO substrate. Furthermore, there are small spaces between the CoPi slabs and the FTO surface. These structural defects between CoPi regions and especially between CoPi and the FTO may cause easier delamination and hence explain the lower stability of the PED-CoPi film compared to the AACVD + ET-CoPi. Charge transfer is also adversely affected compared to the densely packed conformal AACVD + ET-CoPi as evidenced by the lower 1.53 mA cm^{-2} current density for (PEC)-CoPi on $BiVO_4$ for sulphite oxidation compared to 1.83 mA cm^{-2} for (AACVD + ET)-CoPi on $BiVO_4$. Furthermore, bubble formation in the case of PED-CoPi films may be expected to preferentially occur at the large gaps

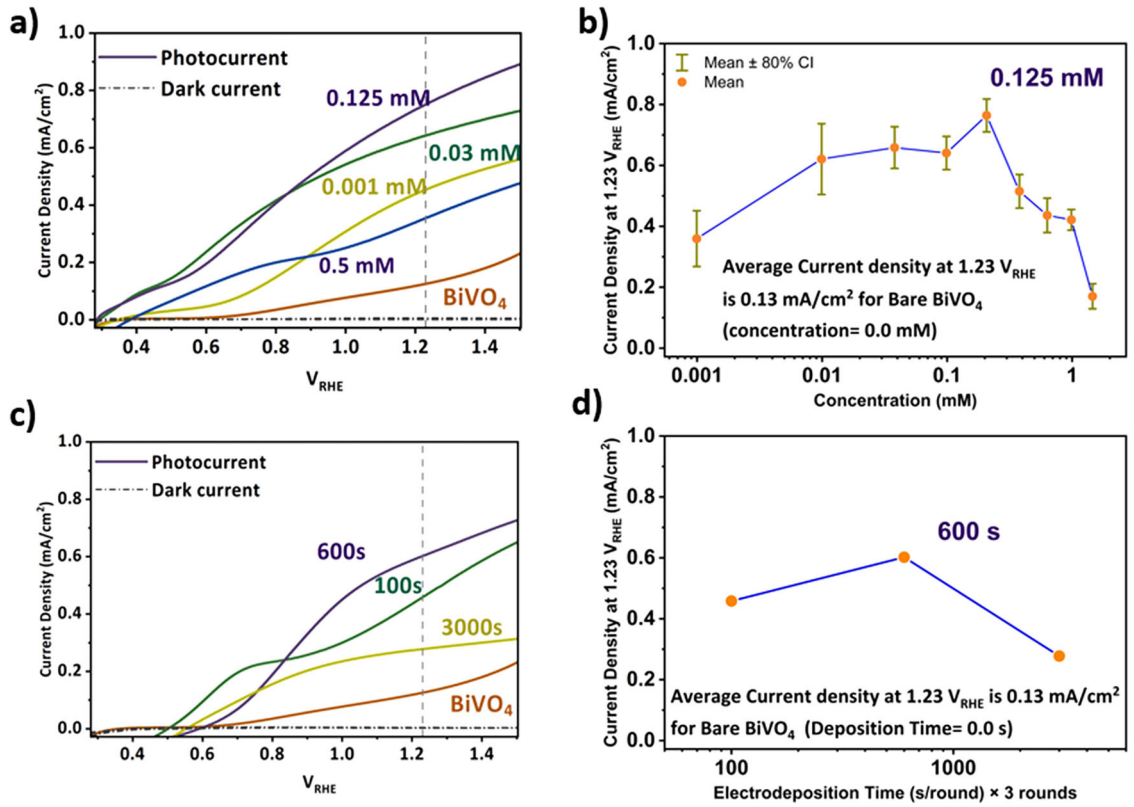

Fig. 3 PEC performance under (front) illumination and dark conditions in borate buffer for (AACVD + ET)-CoPi/$BiVO_4$ deposited from cobalt oxide precursor solutions with concentration indicated. a Selected J–V curves in borate buffer and **b** mean ± 80% confidence interval (CI) current densities measured at 1.23 V_{RHE} from measurements on 3–5 independent samples. 95% confidence intervals are shown in Fig. S14. PEC performance of (PED)-CoPi/$BiVO_4$ with (**c**) J–V curves at deposition durations shown (total of 3 PED cycles per sample). **d** Current density extracted from 1.23 V_{RHE} in borate buffer for (PED)-CoPi/$BiVO_4$ photoanodes.

in the catalyst, letting larger bubbles to aggregate, whereas the (AACVD + ET)-CoPi film may encourage more disperse and ultimately smaller bubble formation which should encourage a more stable photocatalytic performance. In Fig. 2d, XRD measurement is unable to detect crystalline phases of CoO_x, nor of crystalline cobalt phosphate (Figure S9). In Fig. 2e, the (PED)-CoPi/FTO Raman spectrum exhibited peaks at 183 cm^{-1}, 462 cm^{-1}, and 650 cm^{-1}, with peaks between 509 and 590 cm^{-1} associated with Co–O stretching vibrations. The broader Co_3O_4 peaks observed in (PED)-CoPi/FTO, compared to (AACVD + ET)-CoPi, suggest a more amorphous structure. This interpretation aligns with their XRD and SEM analyses, which showed reduced crystallinity in PED films. Tabulated in Fig. 2f, EDX spectra (Fig. S10) and XRF spectra (Fig. S11) of PED-CoPi confirmed the presence of both cobalt and phosphorus, although the stoichiometry is uncertain because of variance in the sampling volume of each technique. Figures S12 and S13 show the XPS spectra of (PED)-CoO_x deposited in non-phosphated pH 9 borate buffer solution and (PED)-CoPi respectively. For PED-CoO_x, residual boron from the borate buffer solution is observed along with peaks associated with tin from the FTO. This observation may be through the large cracks that form on the surface of the PED films. (PED)-CoPi is observed to have 14% atomic mass of phosphorous although also 4% of potassium which must have been incorporated from the deposition in potassium phosphate buffer.

Optimising the co-catalyst thickness on $BiVO_4$ photocatalysts

AACVD-fabricated $BiVO_4$ on FTO were deposited with a thickness of approximately 200 nm from 20 mL of precursor solution following previously reported methods[16,23]. To determine the co-catalyst thickness on $BiVO_4$ that achieves optimal PEC performance, a range of CoPi films were synthesised via AACVD on top of $BiVO_4$ substrates by varying the $Co(acac)_2$ precursor concentration. Representative current-voltage (*J–V*) curves and average photocurrents under 1.23 V_{RHE} applied potential for (AACVD + ET)-CoPi in Fig. 3a, b show that precursor concentrations of between 0.03 and 0.125 mM yielded the highest average PEC performance, with 0.125 mM chosen

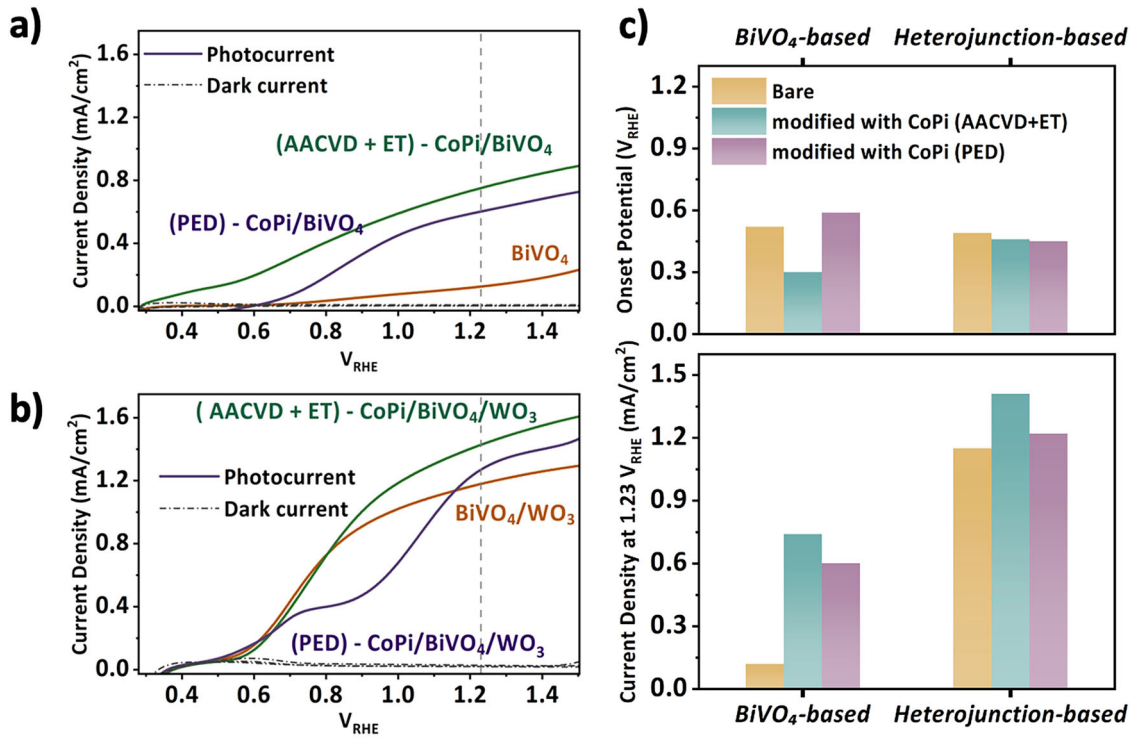

Fig. 4 J–V plots measured in borate buff er under front illumination. J–V plots measured in borate buffer under (front) illumination for comparing (**a**) cocatalysts on bare $BiVO_4$ and **b** co-catalysts on NN $BiVO_4/WO_3$ Heterojunctions, **c** compilation of onset potential and current density at 1.23 V_{RHE} for the samples in **a**, **b**.

for further investigation due to the likely stabilising effect of using a larger amount of co-catalyst. This optimal precursor deposition concentration is calculated to yield films of approximately 2 nm thick, given that a 5 mM precursor concentration was observed to yield an 85 nm-thick film by side-on SEM. Techniques such as high resolution transmission electron microscopy would be required to definitively confirm the thickness and morphology of such thin cocatalyst layers, but as shown in Fig. S1, integration of the current passed during chronoamperometry to convert CoO_x to CoPi is calculated to result in a CoPi layer approximately 1.5 nm thick, corroborating the above estimation.

For PED-CoPi, three thicknesses were prepared on $BiVO_4$ substrates using chronopotentiometry. Thickness was controlled by changing the deposition duration between 100 s, 600 s, and 3000 s per cycle with a total of three cycles conducted in each trial. These conditions yielded CoPi film thicknesses of ~7 nm, ~43 nm, and ~217 nm, estimated by side-on SEM (Fig. 2c for the 3000 s cycle sample). The sample deposited for 600 s exhibited the highest photocurrent density at moderate applied potentials (Fig. 3c, d). The difference in optimal thickness between the (AACVD + ET)-CoPi and (PED)-CoPi on $BiVO_4$ is likely related to morphology of these samples. (PED)-CoPi is grown with wide, deep cracks (Fig. 2c) and therefore water can easily penetrate down to the $BiVO_4$/CoPi interface for larger film thicknesses, which is reported to be integral to its function[8]. The (AACVD + ET)-CoPi is grown as a densely packed layer and is therefore less likely to be as porous for water to penetrate to the $BiVO_4$/CoPi interface, leading to a thinner optimal layer thickness. Specifically, thicker depositions of (AACVD + ET)-CoPi may ultimately be formed of $BiVO_4/CoO_x$/CoPi, where the additional interfaces could hinder the charge transfer dynamics.

PEC performance of AACVD and PED cocatalysts on photoanodes

Linear scan voltammetry (LSV) curves

The LSV curves in Fig. 4a show that films of (AACVD + ET)-CoPi on $BiVO_4$ yielded a more than 6-fold enhancement in photocurrent compared to bare $BiVO_4$ under front illumination in phosphate-free, borate buffered electrolyte, reaching 0.74 mA cm^{-2} at 1.23 V_{RHE}. In contrast, the (PED)-CoPi on $BiVO_4$ fabricated with a 600 s per cycle deposition exhibited a near 5-fold increase, generating a photocurrent density of 0.60 mA cm^{-2}.

In Fig. 4b, the use of nanostructured $BiVO_4$-coated WO_3 photoanode substrates coated with (AACVD + ET)-

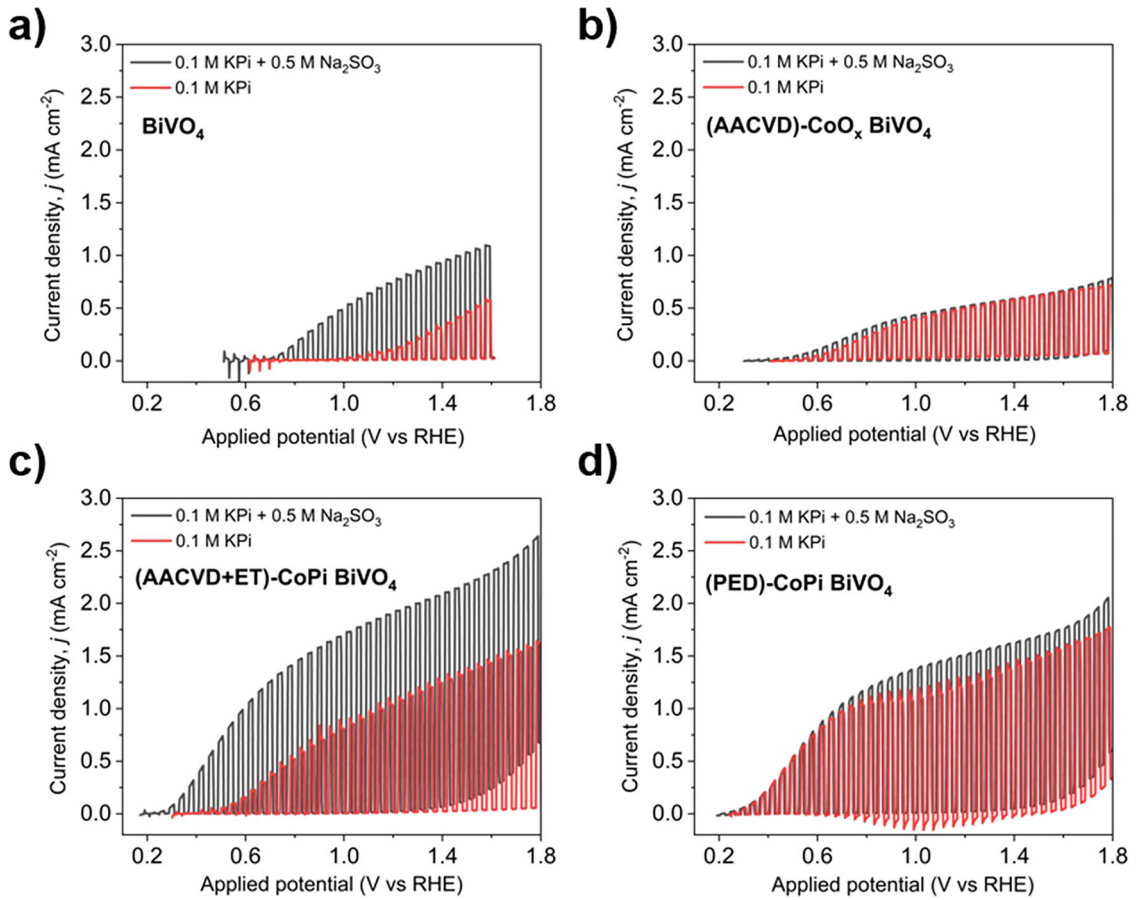

Fig. 5 Chopped LSV curves for water and sulfi te oxidation on $BiVO_4$ photoanodes. **a** without a co-catalyst, **b** with (AACVD)-CoO_x, **c** with (AACVD + ET)-CoPi (C), and with (PED)-CoPi. All measurements were taken under 1 sun (100 mW cm^{-2}, AM 1.5 G) simulated sunlight under back illumination, with a chopping frequency of 1 Hz and scan rate of 20 mV/s.

CoPi increased photocurrent density by 20% from 1.15 to 1.41 mA cm^{-2} at 1.23 V_{RHE}. Similarly, 1.23 mA cm^{-2} was achieved with (PED)-CoPi on a nanostructured $BiVO_4$-coated WO_3 photoanode. However, the photocurrent onset potential remained relatively unchanged for both methods.

All photocurrent onset potentials and current densities at 1.23 V_{RHE} are compiled in Fig. 4c for comparison and shown in the Supplementary Information Fig. S14. The onset potential for the (AACVD + ET)-CoPi on $BiVO_4$ shifted cathodically by approximately 0.2 V compared to the bare $BiVO_4$. This shift is likely due to a reduction in the water oxidation overpotential, introduced by CoPi, which facilitates improved charge separation and mitigates surface recombination losses. Conversely, the PED-fabricated sample showed approximately the same photocurrent onset potential as $BiVO_4$. At modest applied potentials of 1.0 V_{RHE}, the photocurrents of (AACVD + ET)-CoPi on $BiVO_4$ exceeds that of (PED)-CoPi on $BiVO_4$ and both far exceed the photocurrent of bare $BiVO_4$. There is minimal variation in onset potentials observed for the heterojunction systems, compared to that of $BiVO_4$. The staggered band alignment at the $WO_3/BiVO_4$ interface facilitates efficient carrier separation[24], diminishing the additional impact of surface hole-collecting catalysts like CoPi. The catalytic contribution of surface CoPi is less significant when efficient charge separation is already provided by the $WO_3/BiVO_4$ interface.

One sun (AM 1.5 G) measurements with sodium sulfite sacrificial reagent

To investigate the effect of the co-catalysts on charge transfer, LSV measurements were conducted for each electrode under one sun (AM 1.5 G) illumination for sulfite oxidation to assess the intrinsic photoactivity without being limited by surface reaction kinetics. Figure 5 compares water and sulfite oxidation for $BiVO_4$ electrodes with CoO_x and CoPi co-catalysts. Figure S15 further compares the water oxidation performance for $BiVO_4$ and $WO_3/BiVO_4$ heterojunctions with and without

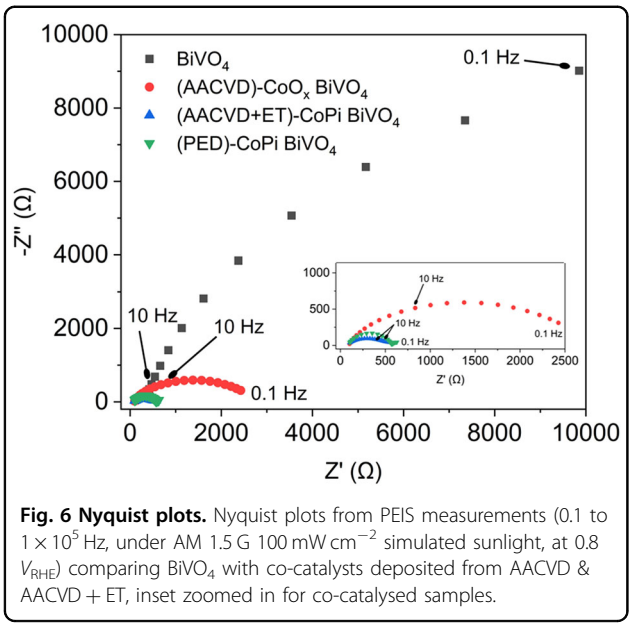

Fig. 6 Nyquist plots. Nyquist plots from PEIS measurements (0.1 to 1×10^5 Hz, under AM 1.5 G 100 mW cm^{-2} simulated sunlight, at 0.8 V_{RHE}) comparing $BiVO_4$ with co-catalysts deposited from AACVD & AACVD + ET, inset zoomed in for co-catalysed samples.

cocatalysts. Both the CoPi co-catalysts (synthesised by AACVD and PED) proved effective in enhancing charge separation, ϕ_{sep} and charge injection, ϕ_{inj} efficiencies compared to bare $BiVO_4$ when conducting sulfite oxidation, with a markedly stronger effect when (AACVD + ET)-CoPi is used. The charge transfer efficiencies, along with the other parameters from Eqs. 5, 6, are summarised in Table S2 for one sun measurements under back illumination.

Figure S16 shows the comparison of water and sulfite oxidation for $WO_3/BiVO_4$ electrodes with CoO_x and CoPi co-catalysts. These electrodes exhibited high charge transfer efficiencies, in line with values reported previously for heterojunction electrodes fabricated by AACVD[25]. The electrodes with CoO_x and CoPi co-catalysts also saw cathodically shifted onset potentials for water oxidation compared to baseline $WO_3/BiVO_4$ electrodes. The incorporation of CoO_x and CoPi co-catalysts on the heterojunction photoanodes also enhanced charge injection (transfer) efficiencies (from the co-catalyst surface to the electrolyte) from 32 % in the heterojunction to 44%with the addition of CoO_x and 86% with the addition of CoPi, with bulk charge separation efficiencies being observed to drop slightly because the photocurrents for sulfite oxidation were unexpectedly lower with the presence of co-catalyst. This decrease in bulk charge separation efficiency was attributed to increased bulk charge transfer resistance arising from additional solid | solid interfaces in the photoanode structure with the incorporation of the co-catalyst. This effect was less detrimental with the incorporation of the PED-synthesised CoPi, likely due to the more conformal coating of the co-catalyst layer afforded by the AACVD method. PEIS measurements (Fig. S17) showed that charge transfer resistance (Table S3) was approximately 16 times lower for the $WO_3/BiVO_4$ heterojunction (at 1.78 kΩ) than for bare $BiVO_4$ (at 28.5 kΩ), providing an already lower baseline for further improvements prior to co-catalyst incorporation. Nevertheless, while charge transfer resistance was further reduced with co-catalysts, the capacitance increased for the (AACVD)-CoO_x and (AACVD + ET)-CoPi co-catalysts relative to the $WO_3/BiVO_4$ baseline value, consistent with the explanation above. Nonetheless, the charge transfer efficiencies of the CoPi-coated $WO_3/BiVO_4$ electrodes are comparable to the 35.0 and 84.6% separation and injection efficiencies of the NiFeOOH-coated $WO_3/BiVO_4$ also fabricated by AACVD by the authors in previous work [26].

Photoelectrochemical impedance spectroscopy

Figure 6 compares Nyquist plots for $BiVO_4$ electrodes with CoO_x and CoPi co-catalysts. Compared to bare $BiVO_4$ electrodes, PEIS analysis showed that the incorporation of the co-catalysts significantly reduced charge transfer resistance (represented by R_{ct} in the equivalent circuit model and evidenced by the increased curvature in Fig. 6). A summary of the equivalent circuit parameters for different $BiVO_4$ based electrodes is provided in Table S3. The charge transfer resistance was lowest with (AACVD + ET)-CoPi and (PED)-CoPi, at 502 Ω and 472 Ω respectively. The addition of co-catalysts also reduced the CPE capacitance compared to bare $BiVO_4$. The capacitance values were lowest when the CoPi co-catalysts were incorporated. With the (AACVD + ET)-CoPi co-catalyst, the capacitance decreased tenfold, to 5.8×10^{-6} F and with the (PED)-CoPi co-catalyst, there was a further decrease, to 1.9×10^{-6} F. This significant drop in capacitance suggests the incorporation of CoPi resulted in the passivation of surface states, widening the depletion region and boosting charge separation.

Stability testing

To evaluate the stability of the CoPi-coated $BiVO_4$ electrodes, chronoamperometry measurements were conducted at a constant potential of 1.23 V_{RHE} under continuous one sun illumination (Fig. 7a). Over four hours, the current density produced by the bare $BiVO_4$ electrodes decreased steadily in line with previously reported $BiVO_4$ photocorrosion effects[27–30]. After testing, the bare $BiVO_4$ electrodes saw a reduction in photocurrent during linear sweep voltammetry of more than 90% at 1.23 V_{RHE}. $BiVO_4$ degradation is typically driven by two mechanisms: the photooxidation of Bi^{3+} ions (which occurs at the commonly used photoanode characterisation potential of 1.23 V_{RHE}) and V^{5+} leaching, which occurs as soon as $BiVO_4$ comes into contact with the electrolyte[28]. Previous studies have demonstrated that co-catalysts can mitigate these effects[26,31], which address Bi^{3+} oxidation by increasing the favourability of water

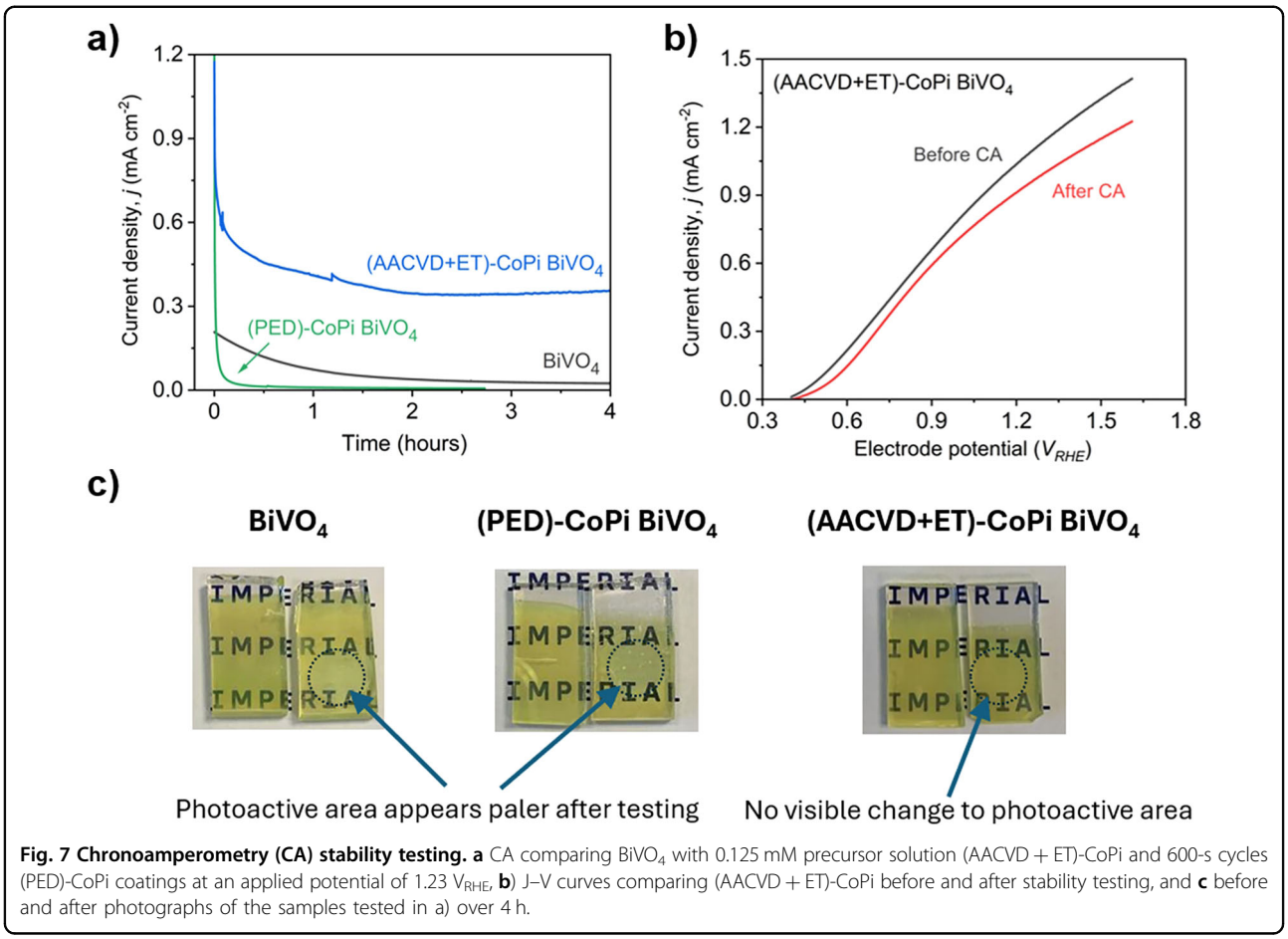

Fig. 7 Chronoamperometry (CA) stability testing. a CA comparing $BiVO_4$ with 0.125 mM precursor solution (AACVD + ET)-CoPi and 600-s cycles (PED)-CoPi coatings at an applied potential of 1.23 V_{RHE}, **b**) J–V curves comparing (AACVD + ET)-CoPi before and after stability testing, and **c** before and after photographs of the samples tested in a) over 4 h.

oxidation kinetics over self-oxidation, and by providing a physical barrier at the $BiVO_4$/electrolyte interface that can suppress V^{5+} leaching. The CoPi co-catalyst fabricated by AACVD appears effective in suppressing $BiVO_4$ degradation, with the photocurrent at 1.23 V_{RHE} retaining near to 90% of its initial value after four hours of chronoamperometry, as shown in Fig. 7b. The drop in photocurrent of the CoPi-coated $BiVO_4$ electrodes during chronoamperometry is attributed to polarisation of the electrode surface. This behaviour is consistent with reports that redox charging and ion accumulation within the CoPi layer under sustained anodic bias temporarily suppress hole injection from $BiVO_4$ into the co-catalyst layer[10,32], which can be reversed by a brief potential sweep or open circuit relaxation. Moderately longer-term stability measurements to the tens of hours would be expected to yield similar stability results, with minor losses in performance possibly arising from gradual CoPi photocorrosion and fragmentation off of the electrode[33], culminating in more rapid performance degradation after a certain proportion of the $BiVO_4$ is exposed. Long-term stability commensurate with commercial applications would need to be demonstrated over hundreds of hours on prototypical devices, as scaled up photoelectrodes would be expected to show different failure modes than laboratory-scale samples.

The (AACVD + ET)-CoPi-coated $BiVO_4$ electrodes were able to recover to near their original performance after chronoamperometry, although the (PED)-CoPi-coated $BiVO_4$ electrodes degraded irreversibly. As with the bare $BiVO_4$ electrode, the photocurrent did not recover after de-polarisation of the electrode and visible changes to the photoactive area are observed after the stability test, as shown in Fig. 7c. After 2.5 h, it was observed that the (PED)-CoPi-coated $BiVO_4$ electrodes showed no photo-activity. This difference between the two deposition methods is attributed to the AACVD procedure resulting in a more homogenous and surface-adhered coating of CoO_x than the cocatalysts fabricated by PED. This manifested in cracks in the (PED)-CoPi layer and spaces between the (PED)-CoPi and FTO (Fig. 2), which may result in a less effective barrier at the $BiVO_4$/electrolyte interface.

Incident Photon-to-Current Efficiency (IPCE) and Half-Cell Solar-to-Hydrogen (HC-STH) Efficiency

Figure 8 presents the IPCE profiles under front-illumination for CoPi-modified $BiVO_4$ photoanodes

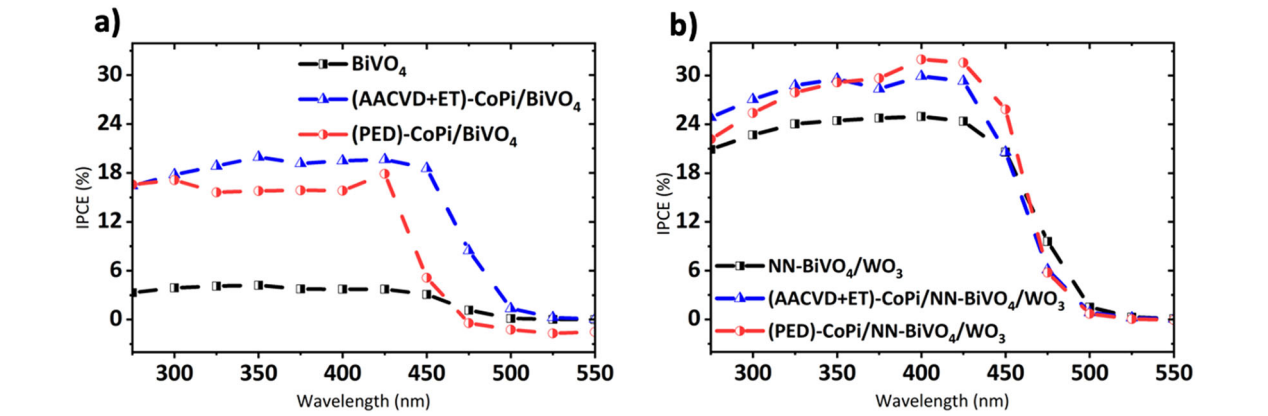

Fig. 8 Incident photon-to-current effi ciency (IPCE) profi les measured in borate buff er under front illumination. **a** flat $BiVO_4$ with CoPi-decoration by AACVD + ET or by PED **b** a NN heterojunction of $BiVO_4/WO_3$ with CoPi-decoration by AACVD + ET or by PED.

fabricated using AACVD + ET and PED. Figure 8a compares CoPi-modified samples on $BiVO_4$ substrates. The (AACVD + ET)-CoPi/$BiVO_4$ photoanode exhibited an average incident photon-to-current efficiency (IPCE) of 19%, representing a near fivefold improvement compared to the bare electrode. Meanwhile, the PED-CoPi/$BiVO_4$ configuration achieved a slightly lower IPCE of 16%, corresponding to a fourfold enhancement. The peak IPCE values for the bare, (AACVD + ET)-modified, and PED-modified $BiVO_4$ electrodes were seen at 400–425 nm, with peak efficiencies of 4%, 20%, and 16%, respectively.

Figure 8b shows the corresponding heterojunction nanostructured (NN) systems compared to (AACVD + ET)-CoPi $WO_3/BiVO_4$, and (PED)-CoPi $WO_3/BiVO_4$, which show higher IPCE compared to the single-layer $BiVO_4$. For illumination at wavelengths between 350 and 425 nm, the (AACVD + ET)-CoPi heterojunction maintained an average IPCE of 29%, reflecting a 1.2-fold enhancement over the NN heterojunction within the same spectral region. The (PED)-CoPi heterojunction showed an even higher average IPCE; approximately 31%. All three heterojunction configurations exhibited peak IPCE values at 400 nm: 25% for the bare, 29% for (AACVD + ET)-fabricated cocatalyst, and 31% for PED-deposited cocatalyst samples.

To evaluate the overall energy conversion potential, the solar predicted photocurrents (SPP) (Equation 3) were used to calculate the HC-STH conversion efficiencies (Equation 4). For bare $BiVO_4$, shown in Fig. 9 below, the SPP was calculated as 0.17 mA cm^{-2}, yielding a HC-STH efficiency of 0.21%. Significant enhancements were observed following CoPi deposition: (AACVD + ET)-CoPi and (PED)-CoPi increased the SPP to 0.94 and 0.49 mA cm^{-2}, corresponding to HC-STH efficiencies of 1.16% and 0.60%, respectively. When integrated into the NN heterojunction structure, further improvements were noted. The (PED)-CoPi/NN heterojunction achieved the highest SPP of 1.34 mA cm^{-2}, followed by 1.19 mA cm^{-2} for the (AACVD + ET)-CoPi/NN heterojunction, and 1.11 mA cm^{-2} for the bare NN heterojunction. The corresponding HC-STH efficiencies for the bare, (AACVD + ET)-, and (PED)-modified heterojunctions were 1.36%, 1.46%, and 1.65%, respectively.

In comparison, (AACVD + ET)-CoPi deposited on flat $WO_3/BiVO_4$ heterojunction yielded an SPP of 1.12 mA cm^{-2} and a corresponding HC-STH efficiency of 1.38%, (Fig. S18) which is an improvement over the bare flat heterojunction that exhibited an SPP of 0.71 mA cm^{-2} and a corresponding HC-STH efficiency of 0.87% but is less effective than the nanostructured photoanodes. A summary of all photoanode performances in 1 M borate buffer in this work is presented in Table 1.

Comparison to reported cobalt cocatalyst-based $BiVO_4$ photoanode systems

In 2023, Chen et al[34]. fabricated a CoO_x film on Fe-doped $BiVO_4$ by drop-casting $Co(acac)_2$ precursor solution, followed by annealing, resulting in a photoanode demonstrating a photocurrent density of approximately 4.0 mA cm^{-2} at 1.23 V_{RHE}. They achieved an IPCE of 54% at 400 nm, which was a threefold enhancement compared to their bare $BiVO_4$[34]. Also in 2023, Varma et al[13]. reported the fabrication of Fe-doped CoO_x co-catalyst layers on $BiVO_4$ photoanodes via photo-assisted electrodeposition. Their optimised photoanode achieved a photocurrent density of 4.6 mA cm^{-2} at 1.23 V_{RHE} [13].

Although the AACVD-fabricated CoPi-decorated $BiVO_4$ system presented in this study exhibits a lower photocurrent density of 0.74 mA cm^{-2} under front-side illumination and HC-STH efficiency of up to 1.5%, it still achieves a 6x enhancement factor over bare $BiVO_4$ samples, and superior stability, demonstrating the

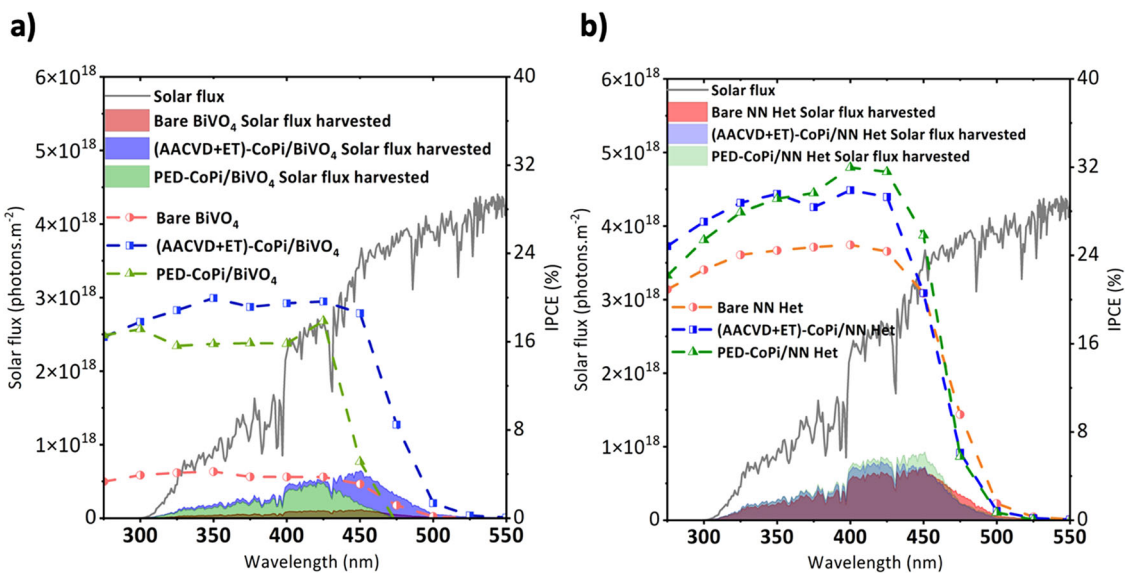

Fig. 9 Incident photon-to-current efficiency (IPCE) and solar predicted photocurrent (SPP) measurements in borate buffer under front illumination. **a** bare $BiVO_4$, (AACVD + ET)-CoPi/$BiVO_4$, and PED-CoPi/$BiVO_4$ photoanodes, and **b** for cocatalysts on $BiVO_4/WO_3$ heterojunctions, illustrating in the shaded regions their solar flux harvested.

Table 1 Summary of photoanode systems tested in 1 M borate buffer in this work.

Photoanode system	PEC synthesis method: (photoanode, cocatalyst)	SPP (mA cm^{-2})	HC-STH (%)
$BiVO_4$	AACVD, n/a	0.17	0.21
CoPi-coated $BiVO_4$	AACVD, AACVD + ET	0.94	1.16
CoPi-coated $BiVO_4$	AACVD, PED	0.49	0.60
NN Heterojunction	AACVD, n/a	1.11	1.36
CoPi-coated NN Heterojunction	AACVD, AACVD + ET	1.19	1.46
CoPi-coated NN Heterojunction	AACVD, PED	1.34	1.65
Flat Heterojunction	AACVD, n/a	0.71	0.87
CoPi-coated Flat Heterojunction	AACVD, AACVD + ET	1.12	1.38
CoPi-coated Flat Heterojunction	AACVD, PED	0.52	0.63

potential of this technique for commercial devices. Moreover, the AACVD fabrication method employed ensures scalability, reproducibility, and cost-effectiveness over conventional methods used for CoPi fabrication (i.e., photo-assisted electrodeposition or drop-casting) and $BiVO_4$ preparation (i.e., spin-coating, spray pyrolysis, or electrodeposition).

Conclusions

An aerosol-assisted chemical vapour deposition and electrochemical treatment (AACVD + ET) technique was developed to grow surface-modified CoPi films to serve as co-catalyst layers on $BiVO_4$ and $BiVO_4/WO_3$ heterojunction photoanodes for application in photoelectrochemical (PEC) water splitting. The physical properties and performance of these CoPi films were compared with those made by a traditional photoelectrodeposition (PED) method. XRD and Raman characterisation suggest that the films first grown by AACVD form a crystalline mixed CoO and Co_2O_3 structure. After electrochemical treatment (ET), linear sweep voltammetry confirmed the catalytic activity of the photoanodes coated with co-catalysts, and chopped light scans in the presence of sulfite oxidation showed that (AACVD + ET)-CoPi on $BiVO_4$ demonstrated the highest charge separation efficiency of 84%, higher than (PED)-CoPi on $BiVO_4$ at 70%. EDX and XRF analysis confirmed the existence of phosphate in (PED)-CoPi films, whereas XPS analysis was required to detect minute amounts of phosphate in (AACVD + ET)-CoPi films, suggesting only surface modification took place. For flat $BiVO_4$ photoanodes coated with CoPi, those grown using AACVD + ET exhibited higher, average IPCE (~19% vs ~16% across the 350–430 nm wavelength range), SPP (0.94 mA cm^{-2} vs 0.49 mA cm^{-2}) and calculated HC-STH efficiencies (1.16% vs 0.60%) compared to (PED)-CoPi on $BiVO_4$. Nyquist plots derived from photoelectrochemical impedance spectroscopy suggest that CoPi deposited by either method provide similarly effective reductions in surface resistance and capacitance. However, only

(AACVD + ET)-CoPi was significantly stable over medium-term continuous operation, retaining more than 90% of its original photocurrent after four hours chronoamperometry, compared with (PED)-CoPi which was totally degraded. This demonstrates the viability of this technique to produce scalable photoanodes.

Acknowledgements
A.K. thanks the EPSRC for a Programme Grant (EP/W017075/1). B.T. thanks the UK Catalysis Meets Plasmonics programme for postdoctoral research funding. We wish to acknowledge the use of the EPSRC funded Physical Sciences Datascience Service hosted by the University of Southampton and STFC under grant number EP/S020357/1. A.H. thanks the Department of Chemical Engineering at Imperial College London for a PhD scholarship for G.C. and a lectureship start-up grant. Lee Tooley, Steve Atkins and Stefanos Karapanagiotidis are thanked for constructing and maintaining our chemical vapour deposition apparatus. Malgorzata Puchnarewicz is thanked for arranging TGA-MS measurements.

Author details
[1]Department of Chemistry, Molecular Sciences Research Hub, Imperial College London, London, UK. [2]Department of Chemical Engineering, Imperial College London, South Kensington, London, UK. [3]London Centre for Nanotechnology, Imperial College London, South Kensington, London, UK

Author contributions
Conceptualisation, B.T. and A.K.; investigation, MH., B.T., G.C., and Z.L.; supervision A.H., B.T., and A.K.; visualisation M.H., G.C., and B.T.; writing—original draft, M.H., G.C., and B.T.; writing review & editing, MH., G.C., Z.L, A.H., B.T., and A.K.

Data availability
The data from this study are available in the tables presented here and in the Supplementary Information.

Competing interests
The authors declare no competing interests.

Ethical approval
Ethics approval was not required for this study because it did not involve human participants or live vertebrate animals.

Publisher's note
Springer Nature remains neutral with regard to jurisdictional claims in published maps and institutional affiliations.

Supplementary information The online version contains supplementary material available at https://doi.org/10.1038/s41427-026-00641-y.

Received: 1 September 2025 Revised: 17 December 2025 Accepted: 24 February 2026
Published online: 18 March 2026

References

1. Calvin, K. et al. *IPCC, 2023: Climate Change 2023: Synthesis Report. Contribution of Working Groups I, II and III to the Sixth Assessment Report of the Intergovernmental Panel on Climate Change [Core Writing Team, H. Lee and J. Romero (Eds.)]. Geneva, Switzerland*. https://doi.org/10.59327/IPCC/AR6-9789291691647. (IPCC, 2023).
2. IEA. The Future of Hydrogen. IEA https://www.iea.org/reports/the-future-of-hydrogen (2019).
3. Moss, B., Babacan, O., Kafizas, A. & Hankin, A. A review of inorganic photoelectrode developments and reactor scale-up challenges for solar hydrogen production. *Adv. Energy Mater.* **11**, 2003286–2003328 (2021).
4. Seabold, J. A., Zhu, K. & Neale, N. R. Efficient solar photoelectrolysis by nanoporous Mo: $BiVO_4$ through controlled electron transport. *Phys. Chem. Chem. Phys.* **16**, 1121–1131 (2014).
5. Rettie, A. J. E. et al. Combined charge carrier transport and photoelectrochemical characterization of $BiVO_4$ single crystals: Intrinsic behavior of a complex metal oxide. *J. Am. Chem. Soc.* **135**, 11389–11396 (2013).
6. Pihosh, Y. et al. Photocatalytic generation of hydrogen by core-shell WO_3 /$BiVO_4$ nanorods with ultimate water splitting efficiency. *Sci. Rep.* **5**, 11141–11150 (2015).
7. Selim, S. et al. WO_3/$BiVO_4$: impact of charge separation at the timescale of water oxidation. *Chem. Sci.* **10**, 2643–2652 (2019).
8. Ma, Y., Le Formal, F., Kafizas, A., Pendlebury, S. R. & Durrant, J. R. Efficient suppression of back electron/hole recombination in cobalt phosphate surface-modified undoped bismuth vanadate photoanodes. *J. Mater. Chem. A* **3**, 20649–20657 (2015).
9. Ma, Y. et al. Rate law analysis of water oxidation and hole scavenging on a $BiVO_4$ photoanode. *ACS Energy Lett.* **1**, 618–623 (2016).
10. Ma, Y., Kafizas, A., Pendlebury, S. R., Le Formal, F. & Durrant, J. R. Photoinduced absorption spectroscopy of CoPi on $BiVO_4$: the function of CoPi during water oxidation. *Adv. Funct. Mater.* **26**, 4951–4960 (2016).
11. Costentin, C. & Nocera, D. G. Self-healing catalysis in water. *Proc. Natl. Acad. Sci. USA* **114**, 13380–13384 (2017).
12. Rekha, P., Yadav, S. & Singh, L. A review on cobalt phosphate-based materials as emerging catalysts for water splitting. *Ceram. Int.* **47**, 16385–16401 (2021).
13. Varma, P. & Reddy, D. A. Promoting the $BiVO_4$ photoanode solar water oxidation performance by coating hole-blocking and oxygen evolution layers. *Energy Fuels* **37**, 7401–7410 (2023).
14. Fang, W., Qin, A., Lin, Y., Xv, R. & Fu, L. A highly enhanced photoelectrochemical performance of $BiVO_4$ photoanodes modified with CoPi groups by increasing energy band bending, accelerating hole separation and improving water oxidation kinetics. *Sustain. Energy Fuels* **6**, 1075–1083 (2022).
15. Kafizas, A. et al. Optimizing the activity of nanoneedle structured WO_3 photoanodes for solar water splitting: direct synthesis via chemical vapor deposition. *J. Phys. Chem. C* **121**, 5983–5993 (2017).
16. Zhao, S. et al. The aerosol-assisted chemical vapour deposition of Mo-doped $BiVO_4$ photoanodes for solar water splitting: an experimental and computational study. *J. Mater. Chem. A* **12**, 26645–26666 (2024).
17. Wong, Y., Li, Y., Lin, Z. & Kafizas, A. Studying the effects of processing parameters in the aerosol-assisted chemical vapour deposition of TiO_2 coatings on glass for applications in photocatalytic NO_x remediation. *Appl. Catal. A Gen.* **648**, 118924–118935 (2022).
18. Coelho, D., Gaudêncio, J. P. R. S. & Mascaro, L. H. Boosting the photocurrent of the WO_3/$BiVO_4$ heterojunction by photoelectrodeposition of the oxyhydroxide-phosphates based on Co, Fe, or Ni. *J. Braz. Chem. Soc.* **33**, 743–752 (2022).
19. National Renewable Energy Laboratory. Reference Air Mass 1.5 Spectra. https://www.nrel.gov/grid/solar-resource/spectra-am1.5.html.
20. Melzer, M., Nichenametla, C. K., Georgi, C., Lang, H. & Schulz, S. E. Low-temperature chemical vapor deposition of cobalt oxide thin films from a dicobaltatetrahedrane precursor. *RSC Adv.* **7**, 50269–50278 (2017).
21. Mirzaeian, M. et al. Improvement of the pseudocapacitive performance of cobalt oxide-based electrodes for electrochemical capacitors. *Energies* **13**, 5228–5243 (2020).
22. Gallant, D., Pézolet, M. & Simard, S. Optical and physical properties of cobalt oxide films electrogenerated in bicarbonate aqueous media. *J. Phys. Chem. B* **110**, 6871–6880 (2006).
23. Tam, B., Pike, S. D., Nelson, J. & Kafizas, A. The scalable growth of high-performance nanostructured heterojunction photoanodes for applications in tandem photoelectrochemical-photovoltaic solar water splitting devices. *Chem. Sci.* **16**, 7794–7810 (2025).
24. Su, J., Guo, L., Bao, N. & Grimes, C. A. Nanostructured WO_3/$BiVO_4$ heterojunction films for efficient photoelectrochemical water splitting. *Nano Lett.* **11**, 1928–1933 (2011).
25. Creasey, G. H., Kafizas, A. & Hankin, A. Investigating the beneficial effects of a WO_3 seed layer on the mechanical and photoelectrochemical stability of WO_3|$BiVO_4$|NiFeOOH photoanodes under operational conditions. *MRS Commun.* **15**, 721–730 (2025).
26. Creasey, G. H. et al. Mechanically and photoelectrochemically stable WO_3|$BiVO_4$|NiFeOOH photoanodes synthesised by a scalable chemical vapour deposition method. *J. Mater. Chem. A* **13**, 11585–11604 (2025).

27. Seabold, J. A. & Choi, K. S. Efficient and stable photo-oxidation of water by a bismuth vanadate photoanode coupled with an iron oxyhydroxide oxygen evolution catalyst. *J. Am. Chem. Soc.* **134**, 2186–2192 (2012).
28. Zhang, S. et al. Dissolution of $BiVO_4$ photoanodes revealed by time-resolved measurements under photoelectrochemical conditions. *J. Phys. Chem. C* **123**, 23410–23418 (2019).
29. Toma, F. M. et al. Mechanistic insights into chemical and photochemical transformations of bismuth vanadate photoanodes. *Nat. Commun.* **7**, 12012–12022 (2016).
30. Zhang, S. et al. Different photostability of $BiVO_4$ in near-pH-neutral electrolytes. *ACS Appl. Energy Mater.* **3**, 9523–9527 (2020).
31. Cui, J. et al. 2D bismuthene as a functional interlayer between $BiVO_4$ and NiFeOOH for enhanced oxygen-evolution photoanodes. *Adv. Funct. Mater.* **32**, 2207136–2207148 (2022).
32. Lin, F. & Boettcher, S. W. Adaptive semiconductor/electrocatalyst junctions in water-splitting photoanodes. *Nat. Mater.* **13**, 81–86 (2014).
33. Zhou, Z. et al. Integration of cobalt-phosphate catalyst and titanium dioxide interlayer in the hematite photoanodes to improve photoelectrochemical water splitting for hydrogen production. *Adv. Compos. Hybrid Mater.* **6**, 94–105 (2023).
34. Chen, D.et al.Boosting charge transfer of Fe doping $BiVO_4/CoO_x$ for photo-electrochemical water splitting. *ACS Appl. Energy Mater.***6**, 8495–8502 (2023).